A Representative Volume Element Model for the Adhesion Between a Micro-Pillared Surface and a Compliant Substrate

Madalyn D. Kern[a], Rong Long[a], Mark E. Rentschler[a,*]

[a]*Department of Mechanical Engineering, University of Colorado at Boulder, 1111 Engineering Drive, Boulder, CO 80309*

Abstract

A representative volume element (RVE) model was developed to understand how the adhesion response between an effectively rigid substrate with micro-pillar arrays and a compliant substrate is affected by the spacing and aspect ratio of pillars. A number of verification and validation steps were taken to ensure the RVE model was robust. We found that the pull-off force decreases when pillar spacing is small enough such that the local deformation within the compliant substrate around one pillar is affected by neighboring pillars. Additionally, pull-off force can increase dramatically if the compliant substrate makes contact with the back surface between pillars, which occurs when the pillar spacing is large and pillar aspect ratio is small. Our RVE model can provide useful insights and quantitative data for understanding the adhesive contact mechanics between micro-patterned surfaces and soft substrates.

Keywords: adhesion, micro-pillar, representative-volume-element model

1. Introduction

Surgical robots have the potential to assist surgeons with arduous surgical procedures while also decreasing patient discomfort or pain during a procedure. Our research group has worked to develop an active robotic capsule endoscope (RCE), a diagnostic and therapeutic tool which can make endoscopy and colonoscopy procedures easier for a surgeon and less painful for a patient [1]. Our RCE uses polydimethylsiloxane (PDMS) micro-pillared tread surfaces for mobilization through the large and small bowel organs [2]. We have done experimental testing with the micro-pillared treads to characterize both translational tractive forces [3, 4] and normal adhesive forces [5–7] when in contact with a soft synthetic substrate. However, to further optimize the RCE's mobility and expand the use of micro-pillared surfaces to other applications, we are interested in developing a computational model which can help us understand how the interfacial response may be affected by different pillar geometries.

The mechanics of contact and adhesion has been a major field of study for over a century. It can be dated back to Hertz [8] who developed the first analytical contact mechanics solution for two elastic spheres. The Hertz theory was later extended to account for adhesive interactions at the contacting surfaces, most

---

notably by Johnson, Kendall and Roberts (JKR theory) [9] and Derjaguin, Muller and Toporov (DMT theory) [10, 11]. Since then, numerous models have been developed to accommodate more complex contact geometries or adhesive interactions [12]. In these models, adhesion is typically described through the cohesive zone model, a concept first introduced by Dugdale and Barenblatt [13–15] to include the effect of plastic yielding in fracture mechanics. The simplest cohesive zone model, known as the Dugdale strip yield model [14], assumes a constant stress distribution over the cohesive zone region. However, many more complex cohesive zone models have been presented within the literature, including the bilinear model and exponential model [16, 17].

The purpose of this work is to present a finite element model that captures the contact interface between an effectively rigid micro-pillar array and a compliant substrate. We chose to develop a representative-volume-element (RVE) model to study the interaction. Within the RVE model, adhesion was modeled using a bi-linear cohesive zone model (Figure 1b). Our primary focus was to understand how the pillar array geometry (spacing and height) affects the total adhesion force. The incorporation of lateral friction into this model will be a topic of future investigation.

Over the past decade, there have been many works on gecko adhesion which aim to uncover the various phenomena contributing to a gecko's unique ability to climb up vertical or overhung surfaces [18–27]. Our study is different from the gecko adhesion work because although both realms of work investigate how adhesion is affected when a smooth substrate is in contact with a micro-patterned substrate, the micro-patterned substrate in our study is effectively rigid in comparison to the smooth compliant substrate, whereas the micro-patterned substrate is considered compliant in comparison to the smooth rigid surface it contacts in the gecko adhesion studies. Therefore, our unique contact geometry requires verification and validation of a new finite element model.

This paper is organized as follows. In Section 2 we describe the development of the finite element model and present the parametric study configurations; Section 3 presents the results of the finite element model and the parametric study; a discussion of the parametric study trends and implications are presented in Section 4; and Section 5 summarizes the our conclusions.

2. Computational Model

2.1. Cohesive Zone Model

A cohesive zone model is a stress based model which describes the separation of two contacting surfaces (Figure 1a). It incorporates an adhesion energy term (w) which represents the additional energy that must be supplied to overcome the adhesive attraction between the contacting surfaces. We chose to use a bi-linear cohesive zone model (Figure 1b) in this work for simplicity.

At least three parameters are needed to fully define the bilinear cohesive zone model. The most critical parameter to define is the adhesion energy (w), as this parameter is characteristic to the specific contact interface. It is well-known within the literature that for a given interface, the remaining cohesive zone
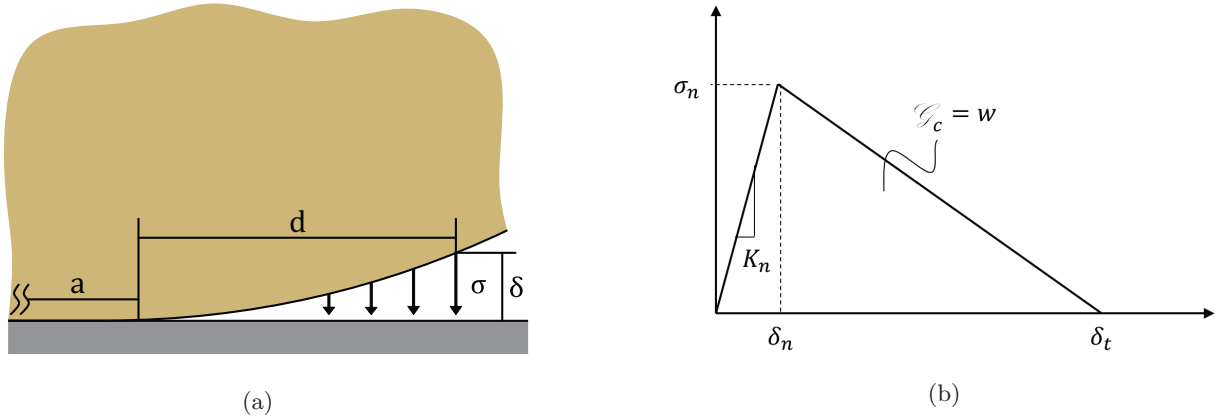
Figure 1: The cohesive zone model defines a finite stress distribution between two contacting surfaces for the region just outside the crack tip ($a \leq r \leq a + d$). In this work we chose to use a bi-linear cohesive zone model.

parameters will have negligible influence on the overall adhesive response as long as the adhesion energy (w) remains consistent and the maximum separation (δ_t) is much smaller than the contact radius (a or R) or other characteristic length scales [17]. We will use this fact as a verification tool for the adhesion interaction model.

2.2. Finite Element Model Development

We are interested in understanding how pillar geometry and relative spacing of an effectively rigid micro-pillared surface affects the adhesion response with a compliant substrate. Due to the length scale of the micro-pillar geometry, running a full quarter symmetry model is not practical from a computational cost perspective. Therefore, we used a representative volume element (RVE) model - a common tool used to reduce a periodic volume to its simplest unit which can yield a representative value of the whole. We chose a triangular cross-section volume element for our RVE model (Figure 2b). The micro-pillared substrate in the RVE model captures one sixth of the pillar geometry at each corner, or, one half of a pillar total (it is important to note that the RVE model neglects the curvature of the spherical indenter as shown in Figure 2b). To understand how various pillar geometry and spacing values affect the adhesion response between the micro-pillared and compliant substrates, we designed a parametric study where pillar geometry and spacing were varied.

To verify and validate the adhesive interaction model used in the RVE model (Figure 2b), we chose to develop a model with a smooth contact geometry (Figure 2a). The particular contact geometry that we chose for the smooth contact model is based on our previous published experimental work [7]. By using the same contact geometry in the smooth contact model as was used experimentally, we were able to compare our finite element model results for the smooth contact model to experimental data for validation.

In each finite element model, both the micro-pillared and compliant substrates (a polydimethylsiloxane (PDMS) material and a PVC plastisol compound, respectively) were modeled as incompressible Neo-Hookean
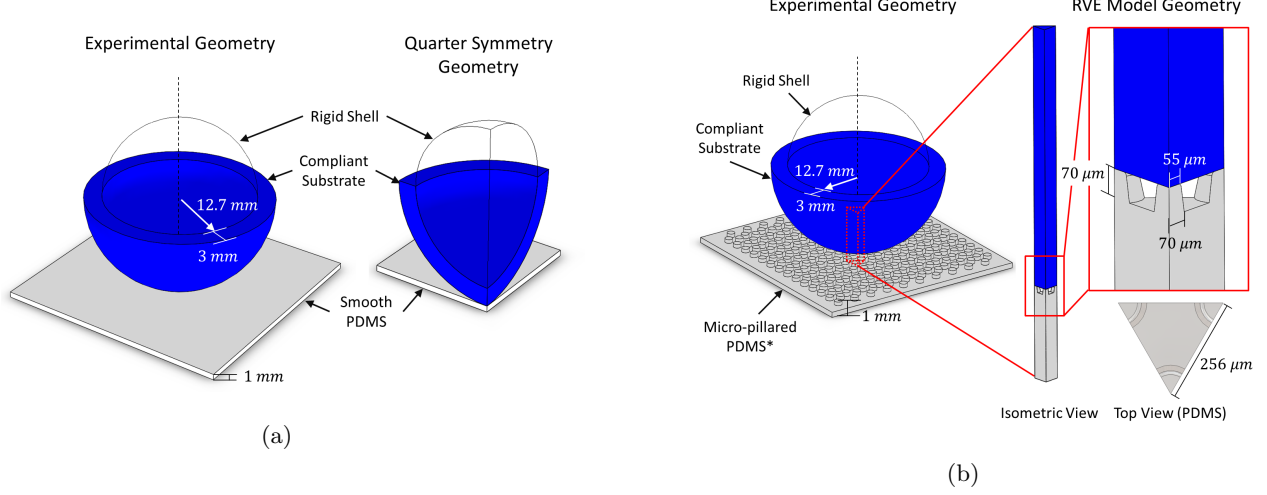
3

Figure 2: Two finite element models were developed using ABAQUS 6.14: (a) 3D quarter symmetry smooth contact and (b) 3D representative volume element (RVE) for micro-pillared contact. *Note: the pillars in the micro-pillared PDMS in Figure 2b are not drawn to scale. Also, the RVE model neglects the curvature of the spherical indenter for simplicity.

Table 1: This table lists the Neo-Hookean material constants $(C_1$ and $D_1)$, corresponding linear elastic parameters $(E$ and $\nu)$ and material densities (ρ) used for the PDMS and compliant substrates.

	C_1 (MPa)	D_1 (MPa)	E (MPa)	ν	ρ (kg/mm^3)
PDMS	0.4833	0	2.9	0.5	9.65×10^{-7}
Compliant Substrate	0.0025	0	0.015	0.5	1.02×10^{-6}

hyperelastic materials. The PDMS elastomer $(10 : 1$ base-to-curing agent weight ratio) can be well described by the neo-Hookean model in the small strain regime [28], which is the case in our system because the PDMS pillars do not undergo significant deformation. Additionally, we have shown through previous experimental work that the PVC plastisol compound (from MF Manufacturing, Fort Worth, TX) behaves elastically within the small strain regime [6]. Both materials were defined with density (ρ) values such that inertial effects could be considered during the simulations. This is necessary because the time during which a crack initiates and propagates during separation can be almost instantaneous. The material constants for each substrate are listed in Table 1.

In each finite element model the PDMS substrate was held fixed while the compliant substrate tied to the rigid shell was displaced linearly. Three steps were defined for each model and each step was defined as a dynamic, implicit step with quasi-static assumptions (dynamic steps were used because of convergence difficulties during separation if static steps were used). The first step initialized contact between the compliant substrate and the PDMS substrate, the second step compressed the compliant substrate onto the PDMS substrate, and the third step retracted the compliant substrate from the PDMS substrate. The time

period defined for each step was determined based on the initial gap size (0.16 mm and 0.071 mm), total compression displacement (1 mm) and strain rate values (0.01 mm/s) for the smooth and micro-patterned contact models, respectively.

The meshing parameters used for each of the finite element models varies slightly due to their geometrical differences. However, in each model, the bulk volume of the PDMS and compliant substrates were meshed using hexahedron shaped elements. In the RVE micro-patten contact model, both the PDMS and compliant substrates used tetrahedral elements near the contact region so that the micro-pattern geometry in the PDMS substrate and the large local deformation in the compliant substrate around the pillars could be resolved. In all cases, linear shape functions were used and the hybrid formulation was required due to the use of hyperelastic material models. Finally, to simplify computational requirements for the PDMS mesh, the PDMS substrate was rigidly constrained. This is an appropriate approximation since the elastic modulus of the PDMS substrate (2.9 MPa) is nearly three orders of magnitude larger than the compliant substrate (15 kPa).

As mentioned in Section 2.1, at least three parameters are needed to fully define the bi-linear cohesive zone model used for the adhesive interaction between the PDMS and compliant substrates. We chose to define the adhesion energy (w), the maximum traction (σ_n) and the contact stiffness (K_n). Of these parameters, w is the only parameter which can be easily extracted through experimental analysis and JKR adhesion theory. In addition, it is the only characteristic parameter for the adhesive interaction; the other two parameters, σ_n and K_n, have negligible influence on the overall adhesion response as long as w remains consistent. Through our previous experimental work in [7], we characterized w for the interface between a PDMS substrate and compliant substrate as 300 mJ/mm^2. Therefore, in this work we used this value for w for both the smooth and micro-patterned contact models and chose various different values for σ_n and K_n for model verification.

2.3. Mesh Convergence and Effect of Cohesive Zone Parameters

2.3.1. Smooth Contact Model

Two different cohesive zone model shapes, Cohesive Zone Model 1 and Cohesive Zone Model 2 (Figure 3), were defined and tested to verify the smooth contact finite element model. For each case, the area under the curve - adhesion energy (w) - was consistent. The finite element model was considered verified when the error in maximum pull-off force between different cohesive zone model cases was less than 10%. To ensure mesh convergence, the number of elements used within the cohesive zone length (d) was varied between 1, 3, and 5 elements and this was done for each cohesive zone model shape. The models were considered converged when the error in maximum pull-off force for models done within a cohesive zone model group was less than 5%.

2.3.2. Micro-Patterned Contact Model

For the micro-patterned contact geometry model, two additional cohesive zone model shapes, Cohesive Zone Model 3 and Cohesive Zone Model 4 (Figure 3), were defined and used for verification testing. As
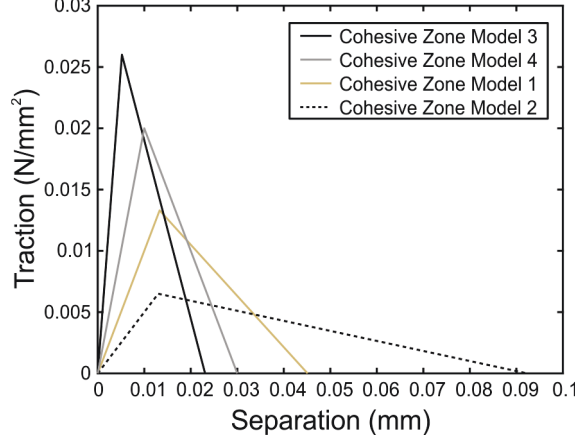
Figure 3: Cohesive Zone Model 1 and 2 were defined and tested to verify the smooth contact geometry model while Cohesive Zone Model 3 and 4 were defined and tested to verify the micro-patterned contact geometry model. For each case, the area under the curve - adhesion energy (w) - remained constant ($w = 3.0 \times 10^{-4}\,\mathrm{mJ/mm^2}$ [7]). The maximum stress (σ_n) and separation stiffness (K_n) are defined as follows for Cohesive Zone Models 1 to 4, respectively: $\sigma_{n,1} = 1.33 \times 10^{-2}\,\mathrm{N/mm^2}$, $K_{n,1} = 1\,\mathrm{N/m^3}$; $\sigma_{n,2} = 6.50 \times 10^{-3}\,\mathrm{N/mm^2}$, $K_{n,2} = 0.5\,\mathrm{N/m^3}$; $\sigma_{n,3} = 2.60 \times 10^{-2}\,\mathrm{N/mm^2}$, $K_{n,3} = 5\,\mathrm{N/m^3}$; $\sigma_{n,4} = 2.00 \times 10^{-2}\,\mathrm{N/mm^2}$, $K_{n,4} = 2\,\mathrm{N/m^3}$.

will be discussed in Section 3.1.2, the two cohesive zone models used for the smooth contact geometry model were not adequate for the micro-patterned geometry because the cohesive zone lengths assumed in the cohesive zone models for the smooth contact geometry were larger than the pillar radii. As with the smooth contact geometry model, the model was considered verified when the error in maximum pull-off force between different cohesive zone model cases was less than 10%. A mesh convergence study was also done for the micro-patterned contact geometry model where the number of elements used within the cohesive zone length (d) was varied at multiple increments between 2 and 40 elements. The models were considered converged when the error in maximum pull-off force for models done with a common cohesive zone model was less than 5%. It should be noted that we chose to scale the pull-off force model output by a factor of 2 such that the results could be presented per pillar rather than half pillar.

2.4. Validation with Experimental Data

While model verification indicates that the physics behind a finite element model are appropriately implemented, it is also important to validate the results of a finite element model by comparing it to experimental data. We chose to use the load displacement results from our previously published experimental work [7] which characterized the adhesion energy for the contact between a compliant substrate and a smooth or micro-pillared PDMS layer. For each contact case, we compared the resultant peak pull-off force from our simulations with the mean experimental peak-pull off force and calculated a percent error.

Table 2: This table lists the nine different configurations of pillar spacing (s) and aspect ratio ($\frac{h}{2r}$) that were built and simulated using the RVE finite element model. *The pillar radius (r) was kept constant at 0.070 mm while the pillar height (h) was varied.

Configuration	1	2	3	4	5	6	7	8	9
Pillar Spacing (s)		0.128 mm			0.256 mm			0.512 mm	
Aspect Ratio* ($\frac{h}{2r}$)	0.25	0.5	1	0.25	0.5	1	0.25	0.5	1

2.4.1. Smooth Contact Model

The smooth contact geometry model uses quarter symmetry (Figure 2a), thus the direct load response from the model is scaled by a factor of 4 before it is compared to the experimental value. No such scaling factor is needed for the resultant displacement.

2.4.2. Micro-Patterned Contact Model

Comparing the results of the RVE model to the experimental data for the micro-pillared PDMS contact case is not as straight forward because the contact geometry reflected in the RVE model is fundamentally different from the experimental case in two ways. First, the RVE model itself only captures the contact response for one half of a pillar, meaning that the output response needs to be scaled by a certain number of pillars rather than scaled by symmetry factors as was done for the smooth contact model case. Second, the RVE model assumes both the micro-pillared surface and the compliant substrate are flat and parallel to each other. This is different from the experimental geometry reported in [7]. In Section 3.2.2, we discuss how to account for these differences when comparing our RVE model results with experimental data.

2.5. Parametric Study

To understand how the micro-pillar geometry itself may affect the overall adhesion response, we chose to design a parametric study where pillar spacing and aspect ratio were varied. The pillar aspect ratio was varied by changing pillar height while holding pillar radius constant. Table 2 lists nine different geometric configurations used for the parametric study. Configuration 5 is considered the nominal case, as the pillar spacing and aspect ratio in this case are identical to what was used in the micro-patterned contact model described previously (Figure 2b).

To remain consistent across all configurations, the compliant substrate was compressed into the micro-patterned substrate until the compressive force reached approximately 6.0×10^{-2} mN. Each configuration used cohesive zone model 3 parameters and we chose to use 3, 4 and 5 elements within the cohesive zone length, corresponding to approximately 6, 8, and 10 elements along the radius of each pillar. A mean pull-off force and standard deviation was calculated for each configuration across the different mesh sizes. If a model was not able to converge before the pull-off force was achieved, it was not considered in the mean calculation. It should be noted that we chose to scale the pull-off force model output by a factor of 2 such that the results could be presented per pillar rather than half pillar.
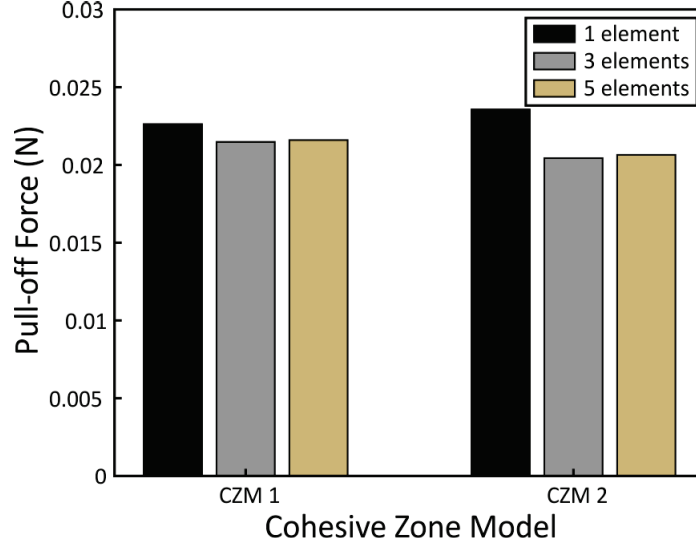
Figure 4: This figure shows the maximum pull-off load simulation results for the smooth contact geometry model for both cohesive zone models at each mesh convergence level.

3. Results

This section presents the results of the verification and validation testing for both our smooth and micro-pillared contact geometry models. It also presents the results of the parametric study done with the micro-pillared contact geometry model.

3.1. Mesh Convergence and Effect of Cohesive Zone Parameters

To ensure the overall adhesion response from the FEA models were independent of specific cohesive zone model shape - given the adhesion energy (w) remained constant among the different cohesive zone model shapes - we analyzed the peak pull-off force from the FEA models for various cohesive zone model shapes. Additionally, a mesh convergence study was completed by incrementally increasing the number of elements within the cohesive zone length.

3.1.1. Smooth Contact Model

The results of the verification tests for the smooth contact geometry model are shown in Figure 4. We observe that for each cohesive zone model case the percent difference in pull-off force decreases as the element size decreases (number of elements within cohesive zone length increases). The maximum percent difference between the 3 and 5 element cases for both cohesive zone models is 1%, indicating that 3 elements within the cohesive zone length is adequate for mesh convergence. Additionally, the maximum percent error between the different cohesive zone models done with 3 elements within the cohesive zone length is 4.1%. This percent error is within our verification requirements indicating the overall adhesion response is independent of the two different cohesive zone models.
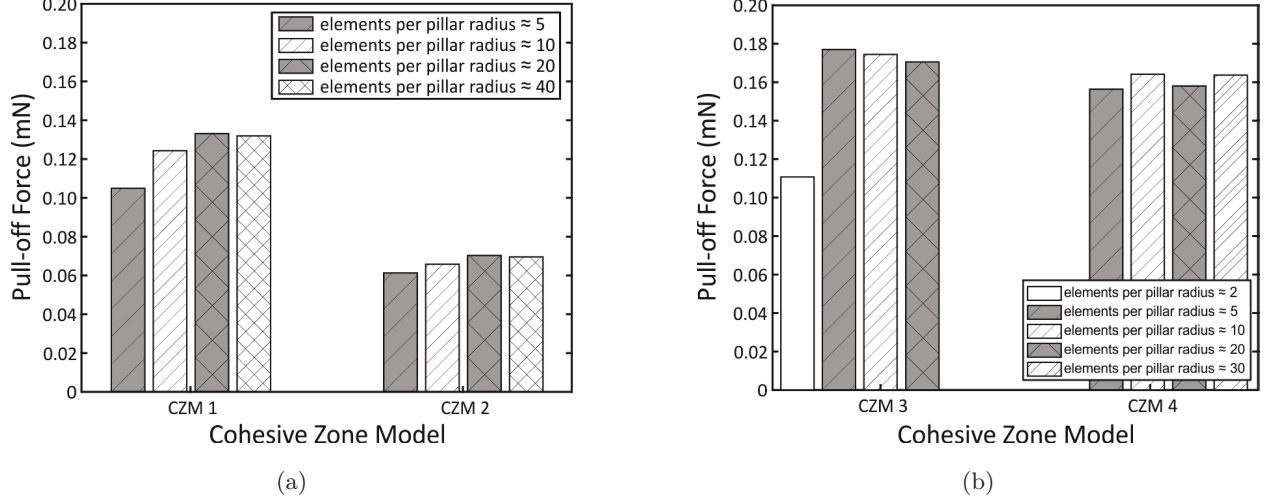
Figure 5: The resultant pull-off force per pillar from the micro-patterned contact geometry model are plotted for various cohesive zone models and mesh sizes. The direct load response from the RVE model is scaled by a factor of 2 so that the results can be interpreted per pillar rather than half pillar.

3.1.2. Micro-Patterned Contact Model

Figure 5a shows the peak pull-off loads per single pillar for the micro-pattern contact geometry model when Cohesive Zone Models 1 and 2 were used. It is clear from the results that the peak pull-off loads per pillar are not consistent between the different cohesive zone models; thus, indicating that the overall adhesion response is not independent of the cohesive zone model. This result can be explained by the fact that the cohesive zone length assumed by these two cohesive zone models is greater than the localized contact length (radius of a single pillar). This directly violates the assumption that the cohesive zone length is much smaller than the contact length ($d \ll a$), a necessary assumption in order for the overall adhesion response to be independent of the cohesive zone model shape.

Therefore, we tested two additional cohesive zone models, Cohesive Zone Model 3 and Cohesive Zone Model 4 (Figure 3), both of which have cohesive zone lengths less than or equal to the the pillar radius. The maximum pull-off loads per pillar for the micro-patterned contact geometry model done with these cohesive zone model shapes are shown in Figure 5b. From these results we observe that as the element size decreases (number of elements per pillar radius increases) the percent difference in the pull-off force per pillar for models with the same cohesive zone model shape decreases. The percent error between the two finest mesh sizes for cohesive zone models 3 and 4 are 1.5% and 3.5%, respectively. Additionally, we observe that the percent difference in pull-off force per pillar for models done with 20 elements along the pillar radius and different cohesive zone model shapes is approximately 7.6%. All of these percent differences are within our verification limits.
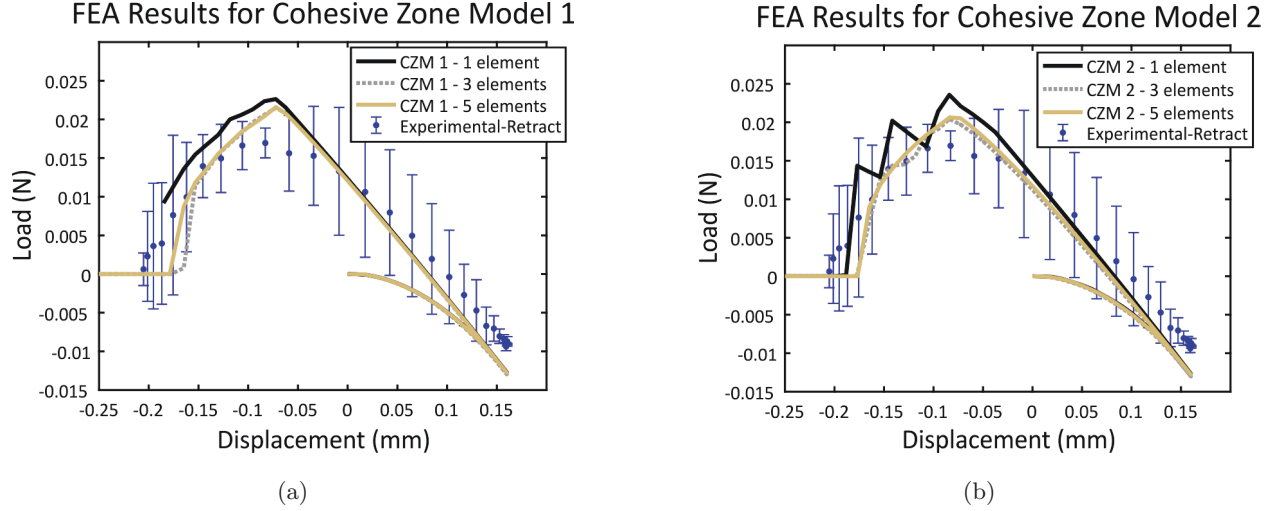
9

Figure 6: The finite element load-displacement results for cohesive zone models 1 and 2 are shown in Figures 6a and 6b, respectively.

3.2. Validation with Experimental Data

The smooth and micro-patterned contact geometry models were validated using experimental data that was collected for adhesion energy characterization [7]. As described in section 2.4, the peak pull-off load for each of our simulations was scaled according the symmetry assumptions made for the contact geometry.

3.2.1. Smooth Contact Model

Quarter symmetry was used for the smooth contact model and thus, the resultant pull-off load was scaled by a factor of four. The resultant displacement did not need to be scaled because the symmetry planes and direction of imposed displacement are parallel. The FEA load-displacement output curves for the first two cohesive zone model configurations are shown in Figure 6. The percent difference between the mean experimental pull-off force and that approximated with the scaled finite element model is approximately 27% and 22%, for the 5 element case for cohesive zone model 1 and 2, respectively.

3.2.2. Micro-Patterned Contact Model

As mentioned in Section 2.4.2, the scaling factor needed to compare the peak pull-off load from the micro-pillared contact geometry model to experimental results is not as straight forward as it is for the smooth contact geometry model. The micro-pillared contact model computes the adhesion response for a unit cell area which in total represents one half of a pillar (three, one-sixth pillars). Therefore, the load response needs to be multiplied by a factor of two to achieve pull-off force per pillar. Then it can be scaled by a given number of pillars which corresponds to the experimental geometry to recover the total pull-off force. However, the given number of pillars cannot simply be the total number of pillars in the contact region between the compliant and micro-pillared substrates because our experimental data comes from a curved compliant substrate contacting a planar micro-pillared substrate (Figure 2b).

10

JKR contact theory suggests that there will be a high stress concentration at the edge of the contact region between a spherical probe and planar substrate. Additionally, it is reasonable to expect that at a certain contact radius, the stress concentration at the edge will trigger the instantaneous failure of the entire adhesive interface. This behavior has been observed for the contact between compliant pillars and a rigid spherical probe and has been described through spring contact theory [29, 30]. While our experimental contact geometry differs from that used to develop JKR contact theory and spring contact theory, the origin for stress concentration in both theories is the curvature at the interface. Therefore, by using the number of pillars around the perimeter of the contact area at the peak pull-off force to scale the RVE model, we can better approximate the experimental response.

Calculating the number of pillars around the perimeter of contact is non-trivial because it is dependent on where the sphere initially contacts the micro-pillared array. We chose to approximate an upper and lower bound for the number of pillars around the contact region when the peak pull-off force was reached. For our upper-bound approximation, we assumed that the pillars were radially distributed (center-to-center pillar spacing of 0.256 mm) and the contact center was the center of the inner-most pillar. The number of pillars around the outer-most ring at the critical radius (where the peak load is observed) is approximately 40 pillars. For our lower-bound approximation, we chose to use one half the number of pillars (20 pillars) due to the fact that the pillars are hexagonally packed in reality. A hexagonal packing factor means that the circular contact edge will either completely miss a pillar along the critical contact radius edge or it will have partial contact with the pillar. Figure 7 illustrates the upper and lower bound peak pull-off forces as well as a peak pull-off force which has been scaled by the total number of pillars in the contact region. When scaling the peak load by either the upper or lower bound for the number of pillars along the contact perimeter, the percent error in the peak load from the RVE model and experimental is 60% and 19%, respectively. While there is still error in these upper and lower bound approximations, the percent error is much less than when the number of pillars within the total contact area is used ($\approx 400\%$ error). Additionally, the experimental pull-off force falls between the upper and lower bound approximations.

3.3. Parametric Study

The mean pull-off force per pillar for each of the nine RVE model configurations is shown in Figure 8a. The standard deviation of the mean is depicted in the error bars at the top of each bar. Figure 8b shows the same pull-off force data as in Figure 8a, only the y-axis is truncated to 0.20 mN to show a more detailed comparison between some of the configurations. From Figure 8b we observe that the pillar spacing only affects the pull-off force significantly if the pillars are very close together (0.128 mm). In this case, the pull-off force is generally less than it is for the other two pillar spacing cases (0.256 mm and 0.512 mm).

The results of the parametric study can also be interpreted through apparent pull-off stress (Figure 9). In this case, the mean pull-off forces (directly from the RVE models) are divided by the apparent contact area over which they act. For each of the different pillar spacing configurations, the apparent area is different because the apparent area is calculated from the base triangular area on which the pillars sit (Figure 2b).
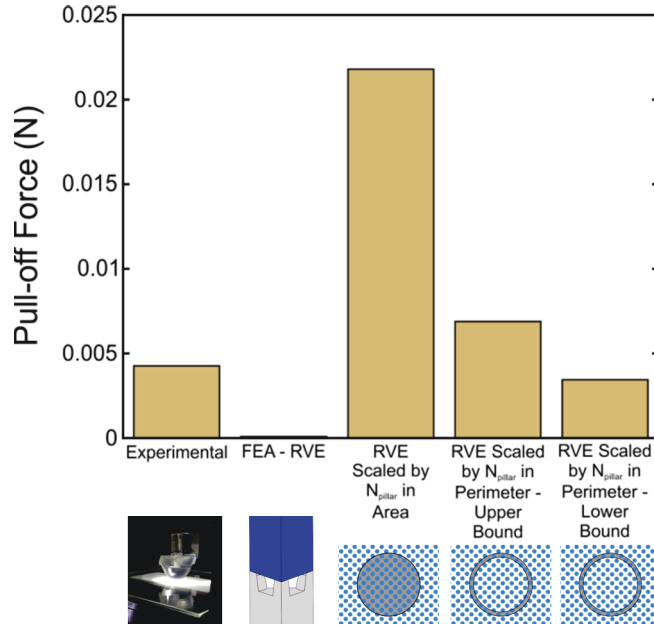
11

Figure 7: This figure compares the peak pull-off force for the representative volume element (RVE) micro-pillared contact model with various scaling factors and experimental data. The "FEA-RVE" configuration is the direct RVE output and therefore the maximum pull-off force per half pillar. The "RVE Scaled by N_{pillar} in Area" configuration is the RVE output scaled by a factor of 252 and therefore the maximum pull-off force per 126 pillars. The "RVE Scaled by N_{pillar} in Perimeter Upper Bound" is the RVE output scaled by a factor of 80 and therefore the maximum pull-off force per 40 pillars. The "RVE Scaled by N_{pillar} in Perimeter Lower Bound" is the RVE output scaled by a factor of 40 and therefore the maximum pull-off force per 20 pillars.
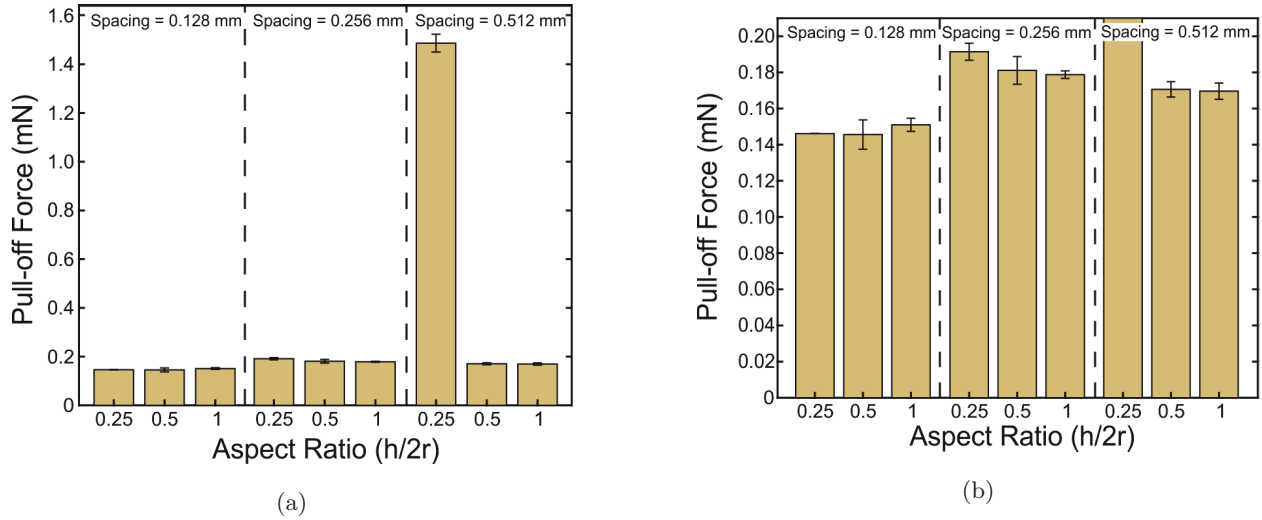

(a)

(b)

Figure 8: This figure shows the mean pull-off force per pillar for each parametric study configuration (direct RVE output response is multiplied by a factor of two since the RVE model geometry is for a half pillar). The mean is calculated from three finite element configurations done with 3, 4 and 5 elements within the cohesive zone length. Figure 8b is simply a zoomed in version of Figure 8a.
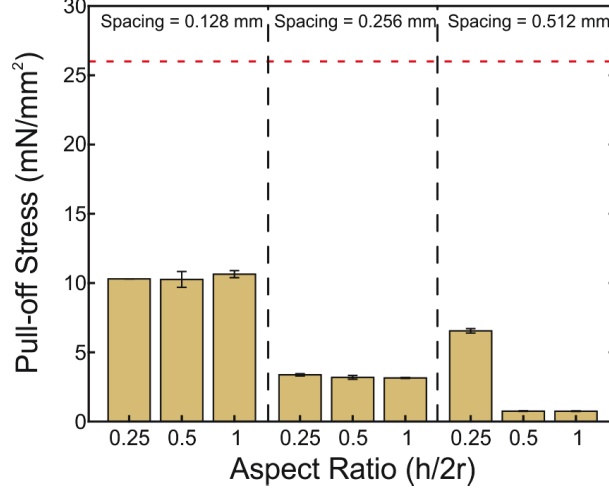
Figure 9: This figure shows the mean apparent pull-off stress for each parametric study configuration. The stress is calculated by dividing the mean pull-off load by the total apparent contact area for each configuration. The horizontal dashed line indicates the maximum possible theoretical cohesive stress based on the cohesive zone model used for the parametric study ($\sigma_n = 2.6 \times 10^{-2}\,\mathrm{N/mm^2}$).

Additionally, we have added a horizontal dashed line to indicate the maximum possible theoretical cohesive stress. In theory the maximum cohesive stress occurs when there are no pillars and the surface is perfectly flat. Therefore, the maximum theoretical cohesive stress can be approximated by the peak of the cohesive zone model which was used in the parametric study ($\sigma_n = 2.6 \times 10^{-2}\,\mathrm{N/mm^2}$).

As observed in Figure 9, as the pillar spacing increases, the apparent pull-off stress decreases. It should be noted that the apparent pull-off stress is simply an averaged stress at the interface of the two contacting materials or the stress that is experienced by the bulk compliant substrate. If we were to consider the stress directly at the interface between the compliant substrate and the PDMS pillars, the stress distribution would be highly non-uniform and may not change between the two larger pillar spacing cases (0.256 mm and 0.512 mm) because the true contact area remains the same and the pillars are far enough apart that they are not locally influencing one another. On the other hand, because we see a decrease in the pull-off force for the case where the pillars are very close (0.128 mm), we may expect to see a net decrease in the local stress distribution around each pillar for this pillar spacing configuration.

The pull-off force and apparent pull-off stress are only influenced by aspect ratio when the pillar spacing is large (0.512 mm) and pillar aspect ratio small (0.25). In this case, the pillars are far enough apart and short enough that the soft synthetic substrate contacts the backing layer between the pillars. Due to the drastic increase in true contact area, both the pull-off force and apparent pull-off stress are increased as compared to the results with the same pillar spacing and larger pillar aspect ratios.
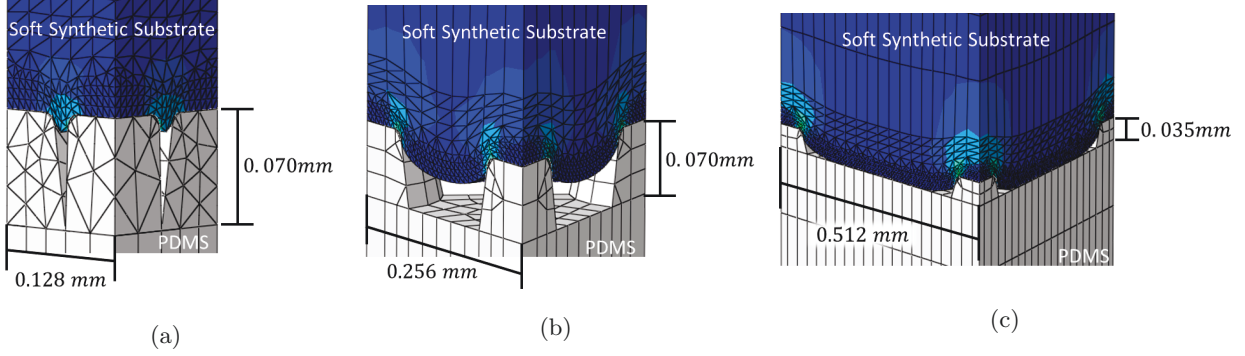
Figure 10: This figure illustrates the local deformation and stress distributions of three different micro-pattern geometry cases.

4. Discussion

The main purpose of this work was to understand how pillar geometry (spacing and aspect ratio) affects the adhesive response between an effectively rigid micro-pillared substrate contacting a smooth compliant substrate. We did an in-depth verification and validation analysis of both a smooth and micro-pillared contact model before completing the the parametric study. The RVE model used for the micro-pillared model assumes some simplifications as compared to the experimental contact geometry. However, we showed that the experimental data falls within a reasonable upper and lower bound approximation from our RVE model. The uncertainty in the RVE model output is a limitation of this work; however, it does not affect our ability to extract relative trends and understand how pillar geometry affects the overall adhesive response.

The images in Figure 10 illustrate the local deformation and stress distributions at the contact interface of three of our different parametric study configurations. In each case we see different local deformation and stress distribution behavior. These images are valuable in that they allow us to hypothesize different practical use cases for each configuration.

Figure 10a illustrates the case where pillar spacing is small and pull-off force minimized. From the image, we can also see that the local deformation of the soft substrate between the pillars is small as well as smaller than it is for the cases when the pillars are farther apart (Figures 10b and 10c). Therefore, it is possible that this specific micro-pattern geometry may be useful for applications where the contacting substrate is very soft as it will help reduce large local deformation between the pillars. An example of such application is with electrodes of neural prostheses. A neural prosthesis has electrodes which interface directly with nerve endings throughout the human body or with brain tissue. It is imperative that the electrodes remain in intimate contact with the neural tissue to ensure connectivity. However, because neural tissue is very soft - on the order of $1 - 10$ kPa - it is also important that the local deformation around the pillars is minimized to reduce damage of the tissue.

Figure 10b illustrates the nominal micro-pattern geometry (that which we have used in our previous experimental work for RCE development [1–7]). The penetration of the soft substrate into the space between the pillars without contacting the backing layer helps provide an understanding as to why we have observed

enhanced traction and minimized adhesion when driving a wheel with this micro-patterned substrate over a synthetic soft substrate or biological tissue. If the deformation profile of the soft substrate between the pillars is the primary mechanism for enhanced traction, it suggests that there may be optimal pillar spacings and aspect ratios for specific stiffnesses of contacting substrates.

Finally, Figure 10c illustrates the case where pillar spacing is large and aspect ratio small. In this configuration we see both large local deformation of the soft substrate around the pillar geometry as well as increased total contact area due to the soft substrate contacting the backing layer of the micro-patterned substrate. This particular configuration may be most acceptable when both adhesion and traction are desirable. Additionally, to help reduce damage of the compliant substrate, it may be beneficial for the compliant substrate to be stiffer. An example of an application where this may be useful is for the development of an aortic stent graft which does not require stitches. An aortic stent graft is used to help reinforce the walls of the aortic artery when an aneurysm is present. Currently, the technology requires the use of stitches to hold the stent in place. However, it is possible that by incorporating a micro-patterned surface around the outside of the stent, the micro-pattern could help hold the stent in place and eliminate the need for stitches. The aortic artery is primarily composed of muscular tissue and thus is generally on the order of $0.1 - 1$ MPa.

5. Conclusions

Through this work, we have presented the development of a verified and validated finite element model which can be used to explore how micro-pattern geometry can affect the adhesion response with a more compliant substrate. Our parametric study results for pillar geometry indicate that if pillar radius is kept constant while pillar spacing and aspect ratio are varied, the pull-off force will only be affected for two cases: (1) pillar spacing is small enough where the local stress and deformation around each pillar influences that of neighboring pillars and (2) pillar spacing is large enough and pillar height small enough that the soft substrate contacts the backing layer of the micro-patterned substrate. Additionally, the apparent pull-off stress will generally decrease as pillar spacing increases. However, if there is contact on the backing layer of the micro-patterned substrate, the apparent pull-off stress will increase due to the increased pull-off force. The use of an RVE model is adequate and ideal for determining trends of adhesion response between different pillar geometries.

References

[1] L. J. Sliker, M. D. Kern, J. A. Schoen, M. E. Rentschler, Surgical evaluation of a novel tethered robotic capsule endoscope using micro-patterned treads, Surgical Endoscopy 26 (10) (2012) 2862–2869. `doi:10.1007/s00464-012-2271-y`.
URL `http://link.springer.com/article/10.1007/s00464-012-2271-y`

[2] L. J. Sliker, X. Wang, J. A. Schoen, M. E. Rentschler, Micropatterned Treads for In Vivo Robotic Mobility, Journal of Medical Devices 4 (4) (2010) 041006–041006. `doi:10.1115/1.4002761`.
URL `http://dx.doi.org/10.1115/1.4002761`

[3] L. Sliker, M. Rentschler, The Design and Characterization of a Testing Platform for Quantitative Evaluation of Tread Performance on Multiple Biological Substrates, IEEE Transactions on Biomedical Engineering 59 (9) (2012) 2524–2530. `doi:10.1109/TBME.2012.2205688`.

[4] L. Sliker, M. Kern, M. Rentschler, An Automated Traction Measurement Platform and Empirical Model for Evaluation of Rolling Micropatterned Wheels, IEEE/ASME Transactions on Mechatronics PP (99) (2014) 1–9. `doi:10.1109/TMECH.2014.2357037`.

[5] B. S. Terry, A. C. Passernig, M. L. Hill, J. A. Schoen, M. E. Rentschler, Small intestine mucosal adhesivity to in vivo capsule robot materials, Journal of the Mechanical Behavior of Biomedical Materials 15 (2012) 24–32. `doi:10.1016/j.jmbbm.2012.06.018`.
URL `http://www.sciencedirect.com/science/article/pii/S1751616112001877`

[6] M. D. Kern, J. Ortega Alcaide, M. E. Rentschler, Soft material adhesion characterization for in vivo locomotion of robotic capsule endoscopes: Experimental and modeling results, Journal of the Mechanical Behavior of Biomedical Materials 39 (2014) 257–269. `doi:10.1016/j.jmbbm.2014.07.032`.
URL `http://www.sciencedirect.com/science/article/pii/S1751616114002380`

[7] M. D. Kern, Y. Qi, R. Long, M. E. Rentschler, Characterizing Adhesion between a Micropatterned Surface and a Soft Synthetic Tissue, Langmuir 33 (4) (2017) 854–864. `doi:10.1021/acs.langmuir.6b03643`.
URL `http://dx.doi.org/10.1021/acs.langmuir.6b03643`

[8] H. Hertz, On the Contact of Elastic Solids, in: Miscellaneous Papers, MacMillan and Co., London, England, 1896, pp. 146–162.

[9] K. L. Johnson, K. Kendall, A. D. Roberts, Surface Energy and the Contact of Elastic Solids, Proceedings of the Royal Society of London. A. Mathematical and Physical Sciences 324 (1558) (1971) 301–313. `doi:10.1098/rspa.1971.0141`.
URL `http://rspa.royalsocietypublishing.org/content/324/1558/301`

[10] K. Fuller, D. Tabor, The effect of surface roughness on the adhesion of elastic solids, Proceedings of the Royal Society of London 345 (1975) 327–342.

[11] V. M. Muller, B. V. Derjaguin, Y. P. Toporov, On two methods of calculation of the force of sticking of an elastic sphere to a rigid plane, Colloids and Surfaces 7 (3) (1983) 251–259. `doi:10.1016/0166-6622(83)80051-1`.
URL `http://www.sciencedirect.com/science/article/pii/0166662283800511`

[12] D. Maugis, M. Barquins, Fracture Mechanics and Adherence of Viscoelastic Solids, in: L.-H. Lee (Ed.), Adhesion and Adsorption of Polymers, no. 12 in Polymer Science and Technology, Springer US, 1980, pp. 203–277.
URL `http://link.springer.com/chapter/10.1007/978-1-4613-3093-6_17`

[13] G. I. Barenblatt, The formation of equilibrium cracks during brittle fracture. General ideas and hypotheses. Axially-symmetric cracks, Journal of Applied Mathematics and Mechanics 23 (3) (1959) 622–636. `doi:10.1016/0021-8928(59)90157-1`.
URL `http://www.sciencedirect.com/science/article/pii/0021892859901571`

[14] D. S. Dugdale, Yielding of steel sheets containing slits, Journal of the Mechanics and Physics of Solids 8 (2) (1960) 100–104. `doi:10.1016/0022-5096(60)90013-2`.
URL `http://www.sciencedirect.com/science/article/pii/0022509660900132`

[15] G. I. Barenblatt, The Mathematical Theory of Equilibrium Cracks in Brittle Fracture, in: F. H. v. d. D. a. L. H. T. v. K. H.L. Dryden, G. Kuerti (Ed.), Advances in Applied Mechanics, Vol. 7, Elsevier, 1962, pp. 55–129.
URL `http://www.sciencedirect.com/science/article/pii/S0065215608701212`

[16] K. Park, G. H. Paulino, Cohesive Zone Models: A Critical Review of Traction-Separation Relationships Across Fracture Surfaces, Applied Mechanics Reviews 64 (2011) 060802–1 – 060802–20.
URL `http://citeseerx.ist.psu.edu/viewdoc/download?doi=10.1.1.654.839&rep=rep1&type=pdf`

[17] C. Y. Hui, A. Ruina, R. Long, A. Jagota, Cohesive Zone Models and Fracture, The Journal of Adhesion 87 (1) (2011) 1–52. `doi:10.1080/00218464.2011.538315`.
URL `http://dx.doi.org/10.1080/00218464.2011.538315`

[18] K. Autumn, Y. A. Liang, S. T. Hsieh, W. Zesch, W. P. Chan, T. W. Kenny, R. Fearing, R. J. Full, Adhesive force of a single gecko foot-hair, Nature 405 (6787) (2000) 681–685. `doi:10.1038/35015073`.
URL `http://www.nature.com/nature/journal/v405/n6787/full/405681a0.html`

[19] K. Autumn, M. Sitti, Y. A. Liang, A. M. Peattie, W. R. Hansen, S. Sponberg, T. W. Kenny, R. Fearing, J. N. Israelachvili, R. J. Full, Evidence for van der Waals adhesion in gecko setae, Proceedings of the

National Academy of Sciences 99 (19) (2002) 12252–12256. `doi:10.1073/pnas.192252799`.
URL `http://www.pnas.org/content/99/19/12252`

[20] E. Arzt, S. Gorb, R. Spolenak, From micro to nano contacts in biological attachment devices, Proceedings of the National Academy of Sciences 100 (19) (2003) 10603–10606. `doi:10.1073/pnas.1534701100`.
URL `http://www.pnas.org/content/100/19/10603`

[21] A. J. Crosby, M. Hageman, A. Duncan, Controlling Polymer Adhesion with Pancakes?, Langmuir 21 (25) (2005) 11738–11743. `doi:10.1021/la051721k`.
URL `http://dx.doi.org/10.1021/la051721k`

[22] M. Kamperman, E. Kroner, A. del Campo, R. M. McMeeking, E. Arzt, Functional adhesive surfaces with ”gecko” effect: The concept of contact splitting, Advanced Engineering Materials 12 (5) (2010) 335–348. `doi:10.1002/adem.201000104`.
URL `http://onlinelibrary.wiley.com/doi/10.1002/adem.201000104/abstract`

[23] C.-Y. Hui, N. J. Glassmaker, T. Tang, A. Jagota, Design of biomimetic fibrillar interfaces: 2. Mechanics of enhanced adhesion, Journal of The Royal Society Interface 1 (1) (2004) 35–48. `doi:10.1098/rsif.2004.0005`.
URL `http://rsif.royalsocietypublishing.org/content/1/1/35`

[24] H. Gao, X. Wang, H. Yao, S. Gorb, E. Arzt, Mechanics of hierarchical adhesion structures of geckos, Mechanics of Materials 37 (23) (2005) 275–285. `doi:10.1016/j.mechmat.2004.03.008`.
URL `http://www.sciencedirect.com/science/article/pii/S0167663604000833`

[25] T. Tang, C.-Y. Hui, N. J. Glassmaker, Can a fibrillar interface be stronger and tougher than a non-fibrillar one?, Journal of The Royal Society Interface 2 (5) (2005) 505–516. `doi:10.1098/rsif.2005.0070`.
URL `http://rsif.royalsocietypublishing.org/content/2/5/505`

[26] L. Shen, C.-Y. Hui, A. Jagota, A two-dimensional model for enhanced adhesion of film-terminated fibrillar interfaces by crack trapping, Journal of Applied Physics 104 (12) (2008) 123506. `doi:10.1063/1.3035908`.
URL `http://scitation.aip.org/content/aip/journal/jap/104/12/10.1063/1.3035908`

[27] J. Liu, C.-Y. Hui, A. Jagota, Effect of fibril arrangement on crack trapping in a film-terminated fibrillar interface, Journal of Polymer Science Part B: Polymer Physics 47 (23) (2009) 2368–2384. `doi:10.1002/polb.21834`.
URL `http://onlinelibrary.wiley.com/doi/10.1002/polb.21834/abstract`

[28] T. K. Kim, J. K. Kim, O. C. Jeong, Measurement of nonlinear mechanical properties of PDMS elastomer, Microelectronic Engineering 88 (8) (2011) 1982–1985. doi:10.1016/j.mee.2010.12.108.
URL http://www.sciencedirect.com/science/article/pii/S0167931710005964

[29] M. Schargott, V. L. Popov, S. Gorb, Spring model of biological attachment pads, Journal of Theoretical Biology 243 (1) (2006) 48–53. doi:10.1016/j.jtbi.2006.05.023.
URL http://www.sciencedirect.com/science/article/pii/S0022519306001986

[30] R. D. O'Rorke, T. W. J. Steele, H. K. Taylor, Bioinspired fibrillar adhesives: a review of analytical models and experimental evidence for adhesion enhancement by surface patterns, Journal of Adhesion Science and Technology 30 (4) (2016) 362–391. doi:10.1080/01694243.2015.1101183.
URL http://dx.doi.org/10.1080/01694243.2015.1101183